IEEE Access
Multidisciplinary | Rapid Review | Open Access Journal

Received April 1, 2021, accepted April 13, 2021, date of publication April 19, 2021, date of current version April 27, 2021.

Digital Object Identifier 10.1109/ACCESS.2021.3074067

Triple-Voltage-Vector Model-Free Predictive Current Control for Four-Switch Three-Phase Inverter-Fed SPMSM Based on Discrete-Space-Vector Modulation

CRESTIAN ALMAZAN AGUSTIN[1], JEN-TE YU[2], CHENG-KAI LIN[1], JUNG JAI[1], AND YEN-SHIN LAI[3], (Fellow, IEEE)

[1]Department of Electrical Engineering, National Taiwan Ocean University, Keelung 202, Taiwan
[2]Department of Electrical Engineering, Chung Yuan Christian University, Taoyuan City 32023, Taiwan
[3]Department of Electrical Engineering, National Taipei University of Technology, Taipei 106, Taiwan

Corresponding author: Cheng-Kai Lin (cklin@mail.ntou.edu.tw)

This work was supported by the Ministry of Science and Technology, Taiwan, under Grant MOST-109-2221-E-019-022-MY2.

ABSTRACT The four-switch three-phase (FSTP) inverters are known for their cost-effective advantages and minimal switching losses. However, such inverter topology's progress is lagging due to control constraints and requirements, including voltage vector limitations and parameter perturbations. To overcome the issue, this paper proposes a triple-voltage-vector model-free predictive current control (TVV-MFPCC) for FSTP inverter-fed surface permanent magnet synchronous motor (SPMSM) drives. The proposed TVV-MFPCC uses the principle of discrete-space-vector modulation (DSVM) to increase the voltage vector selections. Three primary voltage vectors, either the same or distinct, are linearly combined to yield the synthesized voltage vectors. A redundant voltage vector reduction scheme is also introduced to lessen calculations by optimally reducing the candidate voltage vectors to sixteen equivalent hybrid switching modes. To improve prediction accuracy, the TVV-MFPCC performs three different current readings and three current difference calculations in each sampling period. Experiments using a TMS320F28379D microcontroller are conducted to compare the performance of the proposed TVV-MFPCC against conventional MFPCC (C-MFPCC) and validate the scheme.

INDEX TERMS Discrete-space-vector modulation, four-switch three-phase inverter, model predictive current control, model-free predictive control, triple-voltage-vector.

I. INTRODUCTION

Surface-mounted permanent magnet synchronous motor (SPMSM) drives have been primarily significant in numerous high-performance applications for their superior features and advantages [1]–[3]. Compared to other machines, SPMSM offers better efficiency, higher power factor, and higher power density, making it energy-effective equipment [4]–[6]. Some well-known methods have been used in the past to attain these valuable features, such as the classical proportional-integral (PI) control, field-oriented control (FOC), and model predictive control (MPC) [7], [8].

MPC has received extensive attention in motor drives due to its inherent flexibility and fast response [9], [10]. It can be divided into two main applications – model predictive torque control (MPTC) [11] and model predictive current control (MPCC), which is the focus of this article.

MPCC is considerably popular due to no tedious weighting factor requirements. The implementation makes it even more straightforward with the direct measurements of the controlled variable *via* sensors. However, to yield a robust control system, the input signal's calibration and reduction of parametric mismatches should be dealt with. For instance, it is revealed in [12] that the unstable dc bus voltage of three-phase converters has led to voltage gain. In [13], [14], optimized current predictions are presented to calculate multiple current measurements. Jeong and Song [15] proposed an online parameter approximation to calculate the instantaneous current and voltage using the least-square method. Although these strategies have shown significant improvements over

The associate editor coordinating the review of this manuscript and approving it for publication was Inam Nutkani.

the conventional MPCC, their implementations are still affected by machine models. Technically, machine parameters are constants, but they change over time with varying operating temperatures, measurement equipment, aging, and other factors. As such, current deviations and static errors between the calculated current and actual values become inevitable [16], [17].

An attractive solution to resolve this issue is the integration of perturbation observers into the predictive plant model. Liu and Zhao [18] conducted a study based on adaptive robust predictive current control to estimate the mismatch of winding inductance and stator resistance, performing parameter deviation analysis. However, with discrete Luenberger disturbance observer, the computational requirements increase with additional control induced into the prediction process. A quadratic Lyapunov disturbance observer is also designed to achieve asymptotic stability of error estimation for PMSM current control [19]. Wang *et al.* [20] proposed a perturbation observer with feedback compensation to calculate inductance and dc bus voltage deviations. However, the parameter estimation algorithm is too complicated and requires heavy calculations.

Some works on synchronous motor drives with predictive controllers have been proposed [21], [22]. A current ripple reduction strategy is presented by Su *et al.* [23] using a finite-state MPCC based on the current locus to detect rotor position, but the detection accuracy is affected by the number of Hall sensors installed therein. In reference [24], a variable weighting factor-dependent scheme is proposed to measure the voltage vector position and magnitude. However, as with the previously discussed solutions, the methods are highly dependent on parameter estimation accuracy. As an alternative, Lin *et al.* [25], [26] introduced a simple yet effective nonparametric method of model-free predictive current control (MFPCC). MFPCC presents a unique variant of MPCC, which eliminates the observer and system model. Instead, the current difference is measured and utilized to predict the current from the lookup table (LUT) of the stored data. The technique effectively mitigates the effects of parameter mismatches and disturbances in the prediction process.

In the widely used conventional MPCC [27], [28], the number of switching states generated from the inverter is limited, resulting in a single voltage vector application. In [29], [30], the discrete space vector modulation (DSVM) is integrated into the MPC as a practical solution to vector constraints. The DSVM takes advantage by increasing the candidate voltage vectors with the synthesis of virtual voltage vectors. Although significant improvements are observed in the prediction accuracy and ripple reduction [31], the implementation of DSVM on model-free predictive controllers to this day, unfortunately, is still unavailable in the literature. Motivated by this situation, the present work focuses on solving the common concern of the four-switch three-phase (FSTP) inverter for motor drive applications, where signal generation is only limited to four switching states. The paper presents a triple-voltage-vector MFPCC based on discrete-space-vector modulation applied to a four-switch three-phase (FSTP) inverter-fed surface-mounted permanent-magnet synchronous motor (SPMSM). The DSVM increases the candidate voltage vectors using simple linear combinations of three primary voltage vectors at an equal and predefined active duty cycle. The combinations of three primary voltage vectors form a new switching state known as the hybrid switching modes. In a nutshell, the following are the contributions of this article:

1) Present a solution for FSTP inverter voltage vector limitations *via* DSVM. Three primary voltage vectors are linearly combined to increase synthesized voltage vectors.
2) A redundant voltage vector reduction scheme is introduced to optimally reduce the number of candidate voltage to 16 hybrid switching modes.
3) A MFPCC based parameter independent controller is adopted to minimize the effect of parameter perturbations.
4) The proposed TVV-MFPCC performs three different current readings and three current difference calculations in each sampling period to effectively improve the accuracy of current prediction.
5) Experimental validations are performed in various operating conditions to assess the stator current response by three performance measures in terms of current ripples, current errors, and harmonic distortions.

The rest of the article is organized as follows: Section 2 introduces the fundamentals of a four-switch three-phase (FSTP) inverter topology. Section 3 illustrates the modeling of the surface-mounted permanent-magnet synchronous motor (SPMSM). The theoretical framework of the model predictive controllers is presented in Section 4. The details of the proposed TVV-MFPCC algorithm are given in Section 5. Section 6 presents a comparative analysis and study of the experimental results. The conclusion is made in Section 7.

II. THE FOUR-SWITCH THREE-PHASE VOLTAGE SOURCE INVERTER TOPOLOGY

Both six-switch three-phase (SSTP) and four-switch three-phase (FSTP) voltage source inverters (VSI) can be applied to three-phase loads to achieve DC-AC conversion. For example, the FSTP VSI is first proposed [32] to minimize components and reduce switching losses in variable speed drive applications.

A typical circuit diagram of an FSTP inverter-fed SPMSM is shown in Fig. 1, where two identical capacitors, C_1 and C_2, are respectively installed at the upper and lower arm of the "c" phase to save two power switches. The voltages across the two capacitors are represented by v_{c1} and v_{c2}, and the dc-link voltage is denoted as v_{DC}. The power switches are made of insulated gate bipolar transistors (IGBT) with anti-parallel diodes. The four switching states in Fig. 1 are listed in Table 1. The variables S_a and S_b represent the switching states corresponding to the a-phase and the b-phase, respectively.

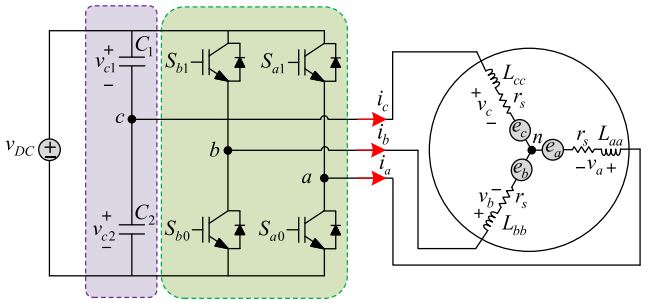

FIGURE 1. A schematic of FSTP Inverter-fed SPMSM.

TABLE 1. Four primary voltage vectors of an ideal FSTP inverter.

Voltage Vectors	Switching States	(S_aS_b)	v_a	v_b	v_c
V_1	S_1	(00)	$-\frac{v_{DC}}{6}$	$-\frac{v_{DC}}{6}$	$\frac{v_{DC}}{3}$
V_2	S_2	(10)	$\frac{v_{DC}}{2}$	$-\frac{v_{DC}}{2}$	0
V_3	S_3	(11)	$\frac{v_{DC}}{6}$	$\frac{v_{DC}}{6}$	$-\frac{v_{DC}}{3}$
V_4	S_4	(01)	$-\frac{v_{DC}}{2}$	$\frac{v_{DC}}{2}$	0

For example, if the variable S_a is 0, the power switch S_{a1} is off, and the power switch S_{a0} is on. Conversely, if the variable S_a is 1, then the power switch S_{a0} is off, and the power switch S_{a1} is on. The same conversion applies to S_b. It should be noted that the power switches S_{a0} and S_{a1} or the power switches S_{b0} and S_{b1} cannot be turned on simultaneously, as the FSTP inverter may be damaged.

Given all possible combinations of S_a and S_b, the phase-wise stator voltage equation can be expressed as

$$\begin{cases} v_a = \left(\frac{2}{3}S_a - \frac{1}{3}S_b\right)v_{c1} + \left(-\frac{1}{3} + \frac{2}{3}S_a - \frac{1}{3}S_b\right)v_{c2} \\ v_b = \left(-\frac{1}{3}S_a + \frac{2}{3}S_b\right)v_{c1} + \left(-\frac{1}{3} - \frac{1}{3}S_a + \frac{2}{3}S_b\right)v_{c2} \\ v_c = \left(-\frac{1}{3}S_a - \frac{1}{3}S_b\right)v_{c1} + \left(\frac{2}{3} - \frac{1}{3}S_a - \frac{1}{3}S_b\right)v_{c2}. \end{cases} \quad (1)$$

Ideally, $v_{c1} = v_{c2} = 0.5v_{DC}$, and the dc-link voltage is $v_{DC} = v_{c1} + v_{c2}$. In this case, the four primary voltage vectors generated from the FSTP inverter can be defined as a function of v_{DC}. Listed in Table 1, these voltage vectors are labeled as V_1, V_2, V_3, and V_4corresponding to switching states of S_1, S_2, S_3, and S_4, respectively.

III. MODELING OF THE SPMSM

A balanced and symmetrical three-phase wye-connected surface-mounted PMSM (SPMSM) is used as a load motor in this study. Under ideal conditions, the mathematical model is described in the stationary reference frames (abc and $\alpha\beta$) to avert arduous rotary coordinate transformations. The equivalent stator voltage equation expressed in continuous-time is written as

$$\begin{bmatrix} v_a \\ v_b \\ v_c \end{bmatrix} = \begin{bmatrix} r_s & 0 & 0 \\ 0 & r_s & 0 \\ 0 & 0 & r_s \end{bmatrix} \begin{bmatrix} i_a \\ i_b \\ i_c \end{bmatrix} + \frac{d}{dt} \begin{bmatrix} \lambda_a \\ \lambda_b \\ \lambda_c \end{bmatrix} \quad (2)$$

where r_s is the stator resistance, i_a, i_b, and i_c are the phase-wise stator currents. λ_a, λ_b, and λ_c are the phase-wise magnetic flux linkages yield from the self-linked flux between stator and rotor interactions. The magnetic flux is further defined as follows:

$$\begin{bmatrix} \lambda_a \\ \lambda_b \\ \lambda_c \end{bmatrix} = \begin{bmatrix} L_{aa} & L_{ab} & L_{ac} \\ L_{ba} & L_{bb} & L_{bc} \\ L_{ca} & L_{cb} & L_{cc} \end{bmatrix} \begin{bmatrix} i_a \\ i_b \\ i_c \end{bmatrix} + \lambda_m \begin{bmatrix} \cos(\theta_e) \\ \cos\left(\theta_e - \frac{2\pi}{3}\right) \\ \cos\left(\theta_e + \frac{2\pi}{3}\right) \end{bmatrix} \quad (3)$$

where L_{aa}, L_{bb}, and L_{cc} are the self-inductances, L_{ab}, L_{ac}, L_{ba}, L_{bc}, L_{ca}, and L_{cb} are the mutual inductances, λ_m is the maximum rotor magnetic flux, and θ_e is the electrical rotor position. Due to symmetry, the following conditions hold

$$\begin{cases} L_{aa} = L_{bb} = L_{cc} = L_s + L_{ls} \\ L_{ab} = L_{ac} = L_{ba} = L_{bc} = ... \\ ..... = L_{ca} = L_{cb} = L_s\cos\left(\frac{2\pi}{3}\right) = -\frac{1}{2}L_s \\ L = L_{ls} + \frac{3}{2}L_s \end{cases} \quad (4)$$

where L_s and L_{ls} are the armature and leakage inductances, respectively. Combining all the above expressions, equation (2) can be expanded into a three-phase voltage equation of the SPMSM as

$$\begin{bmatrix} v_a \\ v_b \\ v_c \end{bmatrix} = \begin{bmatrix} r_s & 0 & 0 \\ 0 & r_s & 0 \\ 0 & 0 & r_s \end{bmatrix} \begin{bmatrix} i_a \\ i_b \\ i_c \end{bmatrix} + L \begin{bmatrix} \frac{di_a}{dt} \\ \frac{di_b}{dt} \\ \frac{di_c}{dt} \end{bmatrix} - \lambda_m\omega_e \begin{bmatrix} \sin(\theta_e) \\ \sin\left(\theta_e - \frac{2\pi}{3}\right) \\ \sin\left(\theta_e + \frac{2\pi}{3}\right) \end{bmatrix} \quad (5)$$

where ω_e is the motor speed. It is noted that the third term of (5) is a sine wave component derived from the product of maximum magnetic flux and motor speed. Such expression is empirically referred to as the back-EMF. We may let $E_m = -\lambda_m\omega_e$. As a result, the phase-wise back-EMF can be deduced as

$$\begin{cases} e_a = E_m\sin(\theta_e) \\ e_b = E_m\sin\left(\theta_e - \frac{2\pi}{3}\right) \\ e_a = E_m\sin\left(\theta_e + \frac{2\pi}{3}\right) \end{cases} \quad (6)$$

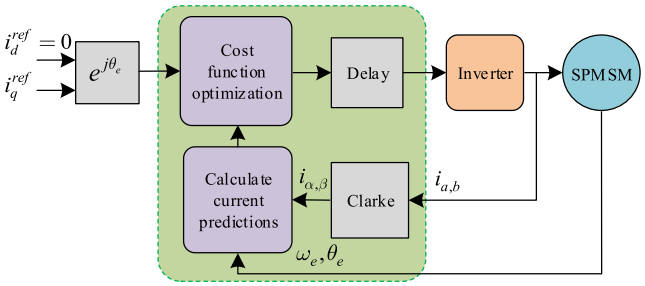

FIGURE 2. A block diagram of MPCC.

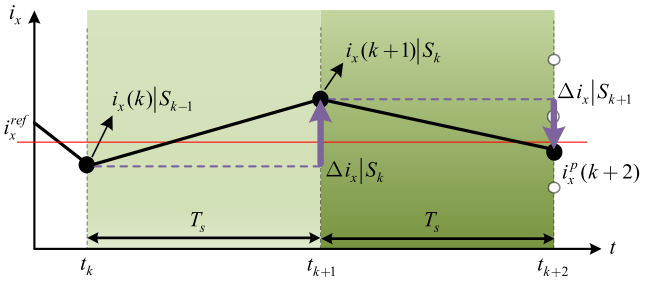

FIGURE 3. A schematic diagram of current predictions in C-MFPCC.

The quantities are redefined to its equivalent stationary two-axis machine model of $\alpha\beta$ *via* Clarke Transformation to simplify the projections. The stator voltage can be written as

$$\begin{cases} v_\alpha = r_s i_\alpha + L\dfrac{di_\alpha}{dt} + e_\alpha \\ v_\beta = r_s i_\beta + L\dfrac{di_\beta}{dt} + e_\beta \end{cases} \tag{7}$$

IV. MODEL PREDICTIVE CURRENT CONTROL

Given below is a brief introduction to the MPCC.

A. THE MPCC

A block diagram of the MPCC is given in Fig. 2. In this method, the controller uses the stator currents as the controlled variable. Based on equation (7), the first-order Euler discretization is employed to yield the instantaneous stator current of the SPMSM at time $k+1$. The current prediction can be written as

$$i_x(k+1) = \left(1 - \frac{r_s T_s}{L}\right) i_x(k) + \frac{T_s}{L}\left(v_x(k) - e_x(k)\right) \tag{8}$$

where $x \in \{\alpha, \beta\}$ and T_s is the sampling period.

Following time delay compensation, the current prediction calculated at $(k+2)th$ period is expressed as

$$i_x^p(k+2) = \left(1 - \frac{r_s T_s}{L}\right) i_x(k+1) + \frac{T_s}{L}\left(v_x(k+1) - e_x(k+1)\right) \tag{9}$$

Under normal circumstances, the sampling frequency is much faster than the rate of stator current change. As a result, the extended back-EMF between two neighboring intervals is assumed to be negligible, that is, $e_x(k) \approx e_x(k+1)$. Finally, for optimality purpose, a cost function, denoted as G, is defined as follows:

$$G = \left|i_\alpha^{ref} - i_\alpha^p(k+2)\right|^2 + \left|i_\beta^{ref} - i_\beta^p(k+2)\right|^2 \tag{10}$$

B. THE CONVENTIONAL MFPCC (C-MFPCC)

The essence of MFPCC is to eliminate the effect of parameter perturbations on the control performance. It is based on the current difference detection technique that uses linear approximations to measure stator currents. Thanks to modern high-speed signal processors, a good approximation of the current difference can be obtained.

A schematic of the C-MFPCC is illustrated in Fig. 3. The notation $i_x(k)|S_{k-1}$ refers to the current measured at $(k)th$ period under switching state S_{k-1}, and $i_x(k+1)|S_k$ is the stator current at $(k+1)th$ period. The current differences are denoted as $\Delta i_x|S_k$ and $\Delta i_x|S_{k+1}$, which are calculated for adjacent switching intervals. At $(k+2)th$ instant, the current predictions are calculated corresponding to different switching states. In FSTP inverters, four possible current predictions are made. The switching state with the least current error is qualified as the optimal one, which will be applied in the next period.

The current differences illustrated in Fig. 3 can be obtained as follows:

$$\begin{cases} \Delta i_\alpha|S_k = i_\alpha(k+1)|S_k - i_\alpha(k)|S_{k-1} \\ \Delta i_\beta|S_k = i_\beta(k+1)|S_k - i_\beta(k)|S_{k-1} \end{cases} \tag{11}$$

and

$$\begin{cases} \Delta i_\alpha|S_{k+1} = i_\alpha(k+2)|S_{k+1} - i_\alpha(k+1)|S_k \\ \Delta i_\beta|S_{k+1} = i_\beta(k+2)|S_{k+1} - i_\beta(k+1)|S_k. \end{cases} \tag{12}$$

Given (11)-(12), the measured stator current at $(k+1)th$ instant can be written as

$$\begin{cases} i_\alpha(k+1)|S_k = i_\alpha(k)|S_{k-1} + \Delta i_\alpha|S_k \\ i_\beta(k+1)|S_k = i_\beta(k)|S_{k-1} + \Delta i_\beta|S_k \end{cases} \tag{13}$$

The current predictions can be expressed as

$$\begin{cases} i_\alpha^p(k+2) = i_\alpha(k)|S_{k-1} + \Delta i_\alpha|S_k + \Delta i_\alpha|S_{k+1} \\ i_\beta^p(k+2) = i_\beta(k)|S_{k-1} + \Delta i_\beta|S_k + \Delta i_\beta|S_{k+1}. \end{cases} \tag{14}$$

V. THE TRIPLE-VOLTAGE-VECTOR MODEL-FREE PREDICTIVE CURRENT CONTROL (TVV-MFPCC)

A common constraint of the FSTP inverter is the number of candidate voltage vectors. A linear combination of three voltage vectors based on discrete space vector modulation (DSVM) is proposed to address the issue.

A. DISCRETE-SPACE-VECTOR MODULATION OF FSTP INVERTER

The DSVM offers an ideal technique to increase the output voltage vectors to any inverter topology [33]. The principle integrates the synthesis of existing primary voltage vectors to form virtual voltage vectors. In the proposed method, three primary voltage vectors are linearly combined to create

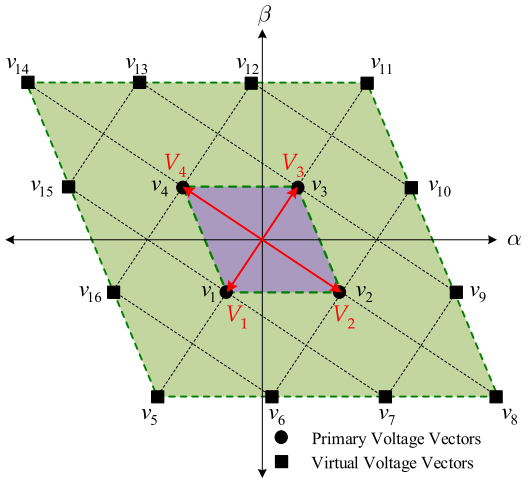

FIGURE 4. The distribution of discrete space vectors of FSTP inverter.

16 synthesized voltage vectors consisting of four primary voltage vectors and twelve virtual voltage vectors. The active time of each switching mode is $T_s/3$, where T_s is the sampling period.

As illustrated in Fig. 4, the virtual voltage vectors are distributed in the primary vectors' outer layer, forming a concentric trapezoidal. The primary voltage vectors are marked as V_1, V_2, V_3, and V_4. The synthesized voltage vectors are derived from the combinations of primary vectors. For instance, v_{10} and v_{12} can be synthesized from the combination of $(V_3V_3V_2)$ and $(V_3V_3V_4)$. The DSVM can yield 64 possible combinations, as shown in Table 2. All these combinations require rolling optimizations but would require considerable computations. However, it can be noticed that some combinations are similar, referring to the same synthesized voltage vectors. A redundant voltage vector reduction scheme is employed herein; for instance, v_1 can be derived from nine possible redundant voltage vector combinations and can be regarded as a single synthesized voltage vector. Applied to the entire DSVM, the candidate synthesized voltage vectors can be significantly reduced to 16 hybrid switching modes only, as described in Table 2.

B. TRIPLE MEASUREMENTS OF STATOR CURRENT AND CURRENT DIFFERENCE

The stator current measurements and the current difference calculations are performed at three separate time instants to improve the prediction accuracy within a given sampling period. The multiple calculation scheme can yield the optimal prediction by taking the average of the three measurements. Each applied synthesized voltage vector's active time is predefined with equal duration to reduce the computational burden.

Shown in Fig. 5 is a schematic of the proposed TVV-MFPCC depicting the three different measurements. In the succeeding sections, the subscript "x" refers to α or β. At the $(k)th$ instant, the three applied switching modes are denoted as $S^h_{k,1}$, $S^h_{k,2}$, and $S^h_{k,3}$, referring to any of the available

TABLE 2. Hybrid switching table derived from DSVM.

Synthesized Voltage Vectors	Hybrid Switching Modes	Redundant Combinations of Primary Voltage Vectors
v_1	S^h_1	$(V_1V_1V_3),(V_1V_3V_1),(V_3V_1V_1),(V_2V_1V_4),(V_2V_4V_1),$ $(V_4V_2V_1),(V_4V_1V_2),(V_1V_4V_2),(V_1V_2V_4)$
v_2	S^h_2	$(V_2V_2V_4),(V_2V_4V_2),(V_4V_2V_2),(V_1V_2V_3),(V_1V_3V_2),$ $(V_3V_1V_2),(V_3V_2V_1),(V_2V_3V_1),(V_2V_1V_3)$
v_3	S^h_3	$(V_3V_3V_1),(V_3V_1V_3),(V_1V_3V_3),(V_2V_3V_4),(V_2V_4V_3),$ $(V_4V_3V_2),(V_4V_2V_3),(V_3V_4V_2),(V_3V_2V_4)$
v_4	S^h_4	$(V_4V_4V_2),(V_4V_2V_4),(V_2V_4V_4),(V_1V_4V_3),(V_1V_3V_4),$ $(V_4V_3V_2),(V_4V_2V_3),(V_3V_4V_2),(V_3V_2V_4)$
v_5	S^h_5	$(V_1V_1V_1)$
v_6	S^h_6	$(V_1V_1V_2),(V_1V_2V_1),(V_2V_1V_1)$
v_7	S^h_7	$(V_2V_2V_4),(V_2V_4V_2),(V_4V_2V_2)$
v_8	S^h_8	$(V_2V_2V_2)$
v_9	S^h_9	$(V_2V_2V_3),(V_2V_3V_2),(V_3V_2V_2)$
v_{10}	S^h_{10}	$(V_3V_3V_2),(V_3V_2V_3),(V_2V_3V_3)$
v_{11}	S^h_{11}	$(V_3V_3V_3)$
v_{12}	S^h_{12}	$(V_3V_3V_4),(V_3V_4V_3),(V_4V_3V_3)$
v_{13}	S^h_{13}	$(V_4V_4V_3),(V_4V_3V_4),(V_3V_4V_4)$
v_{14}	S^h_{14}	$(V_4V_4V_4)$
v_{15}	S^h_{15}	$(V_4V_4V_1),(V_4V_1V_4),(V_1V_4V_4)$
v_{16}	S^h_{16}	$(V_1V_1V_4),(V_1V_4V_1),(V_4V_1V_1)$

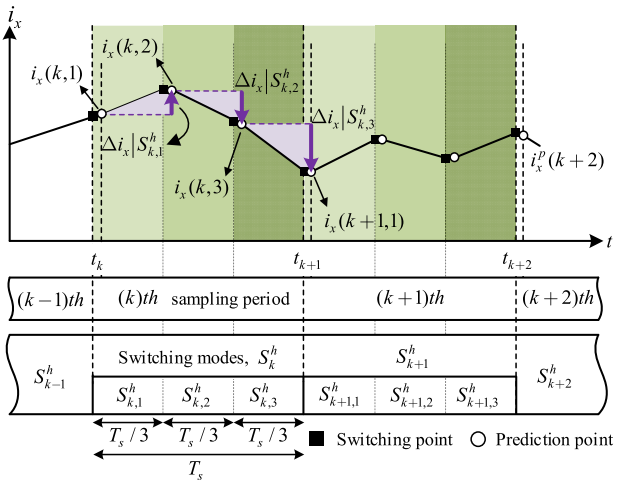

FIGURE 5. A schematic diagram of the proposed TVV-MFPCC.

switching modes. The three stator currents are described as $i_x(k,1)$, $i_x(k,2)$, and $i_x(k,3)$, and their corresponding calculated current differences are depicted as $\Delta\, i_x|\, S^h_{k,1}$, $\Delta\, i_x|\, S^h_{k,2}$, and $\Delta\, i_x|\, S^h_{k,3}$. Corresponding to an applied switching mode, a stator current measurement is performed alongside the current difference calculation. There will be three sets of iterative stator current measurements and current differences stored in the LUT after three switching modes are applied within a given sampling period. The expressions are

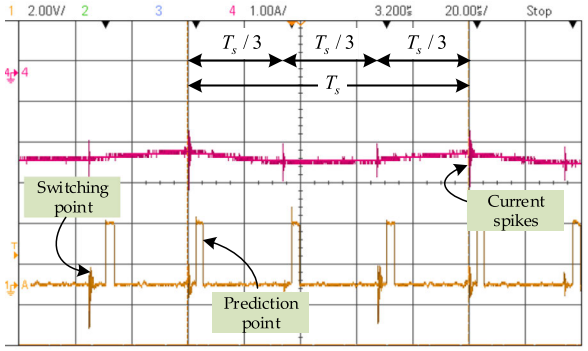

FIGURE 6. Current response under the switching of inverter using the proposed TVV-MFPCC obtained from an oscilloscope.

given as follows:

$$\begin{cases} \Delta i_x|\, S^h_{k,1} = i_x\,(k,2) - i_x\,(k,1) \\ \Delta i_x|\, S^h_{k,2} = i_x\,(k,3) - i_x\,(k,2) \\ \Delta i_x|\, S^h_{k,3} = i_x\,(k+1,1) - i_x\,(k,3) \end{cases} \tag{15}$$

In Fig. 6, it can be noticed that the currents are measured with a short delay after the switching is activated. This strategy is adopted to prevent reading from current spikes.

C. CURRENT PREDICTION AND COST FUNCTION MINIMIZATION

Given the three calculated current differences in each sampling period, the aggregated current differences are not applied immediately. Instead, averaging is employed to get the mean. That is, $\Delta i_x|_k^{T_s}$ and $\Delta i_x|_{k+1}^{T_s}$ can be calculated as

$$\begin{cases} \Delta i_x|_k^{T_s} = \dfrac{1}{3}\left(\Delta i_x|\, S^h_{k,1} + \Delta i_x|\, S^h_{k,2} + \Delta i_x|\, S^h_{k,3}\right) \\ \Delta i_x|_{k+1}^{T_s} = \dfrac{1}{3}\left(\Delta i_x|\, S^h_{k+1,1} + \Delta i_x|\, S^h_{k+1,2} + \Delta i_x|\, S^h_{k+1,3}\right) \end{cases} \tag{16}$$

According to Fig. 5, the two current differences $\Delta i_x|_k^{T_s}$ and $\Delta i_x|_{k+1}^{T_s}$ are calculated in the $(k+1)th$ and $(k+2)th$ instant, respectively. This means that their values are estimated to predict the stator current $i_x^p\,(k+2)$. Since the sampling period T_s is fixed and substantially short, the variation between the adjacent current differences can be considered negligible. As a result, the calculated current difference is used to approximate the future values. The following expressions hold

$$\begin{cases} \Delta i_x|_k^{T_s} \approx \Delta i_x^{pre}|_k^{T_s} \\ \Delta i_x|_{k+1}^{T_s} \approx \Delta i_x^{pre}|_{k+1}^{T_s} \end{cases} \tag{17}$$

where superscript "*pre*" refers to their previous (old) values. As a result, the current prediction equation of the proposed TVV-MFPCC can be rewritten as

$$\begin{cases} i_\alpha^p\,(k+2) = i_\alpha\,(k) + \Delta i_\alpha^{pre}|_k^{T_s} + \Delta i_\alpha^{pre}|_{k+1}^{T_s} \\ i_\beta^p\,(k+2) = i_\beta\,(k) + \Delta i_\beta^{pre}|_k^{T_s} + \Delta i_\beta^{pre}|_{k+1}^{T_s} \end{cases} \tag{18}$$

Similar to (10), the cost function of the TVV-MFPCC is defined for the current error between the $i_x^p(k+2)$ and the i_x^{ref} as

$$G = \left|i_\alpha^{ref} - i_\alpha^p\,(k+2)\right|^2 + \left|i_\beta^{ref} - i_\beta^p\,(k+2)\right|^2 \tag{19}$$

A block diagram of the TVV-MFPCC is given in Fig. 7. The proposed method is started with a current reference command $i_{\alpha,\beta}^{ref}$ *via* the P.I. controller. A current sensor is used to measure the actual stator current in the *a* and *b* terminals of the SPMSM. The three current differences are fed to the predictive module to generate the current predictions for the $(k+2)th$ period. Meanwhile, the initial current difference in the $(k)th$ period is calculated from the previous period.

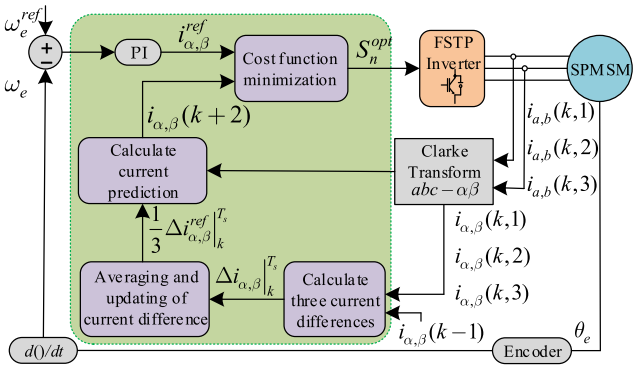

FIGURE 7. A control block diagram of the TVV-MFPCC.

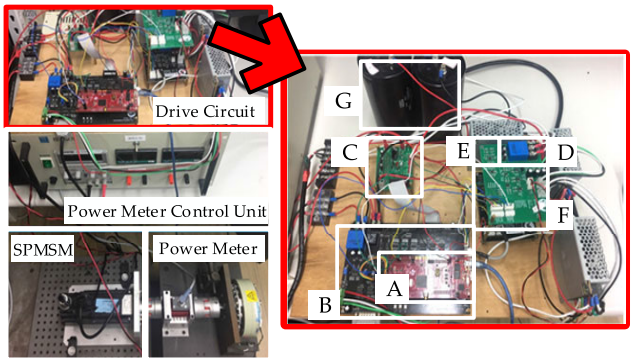

FIGURE 8. Components of the experimental test bench.

TABLE 3. SPMSM specifications.

Parameter	Unit	Value
Rated Power	W	1000
Rated Speed	rpm	2000
Rated Torque	Nm	4.8
Number of Poles	pair	4
Stator Resistance	Ω	1.57
d-axis inductance	*m*H	5.1
q-axis inductance	*m*H	5.1

TABLE 4. Controllers calculation requirement.

Method	Calculation Time	Sampling Time (T_s)
C-MFPCC	32.4 μs	100 μs
TVV-MFPCC	56.8 μs	100 μs

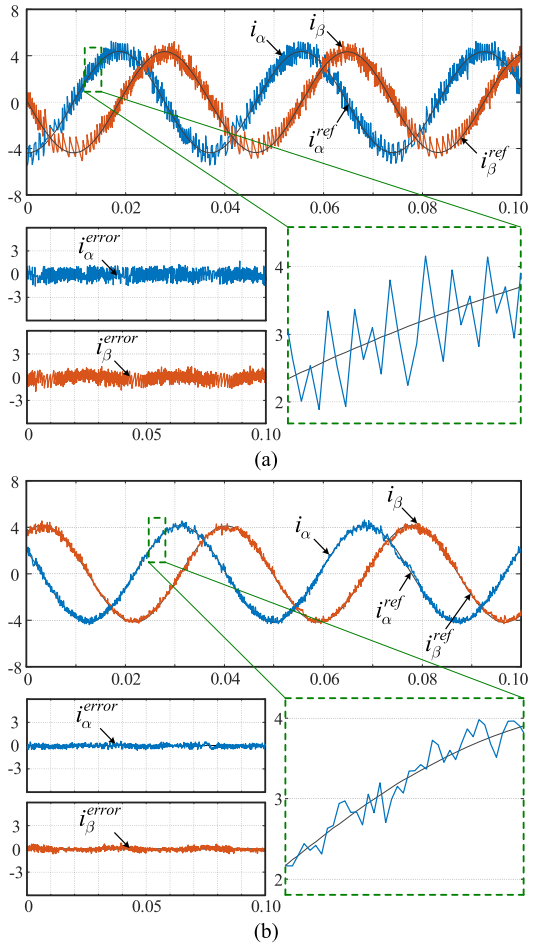

FIGURE 9. Current response under 400 rpm and 3 Nm load-torque, (a) of the C-MFPCC and (b) of the proposed TVV-MFPCC. On the lower left of each part is the $\alpha\beta$ current errors, and on the lower right of each part is the enlarged α-phase current response. Time is in seconds.

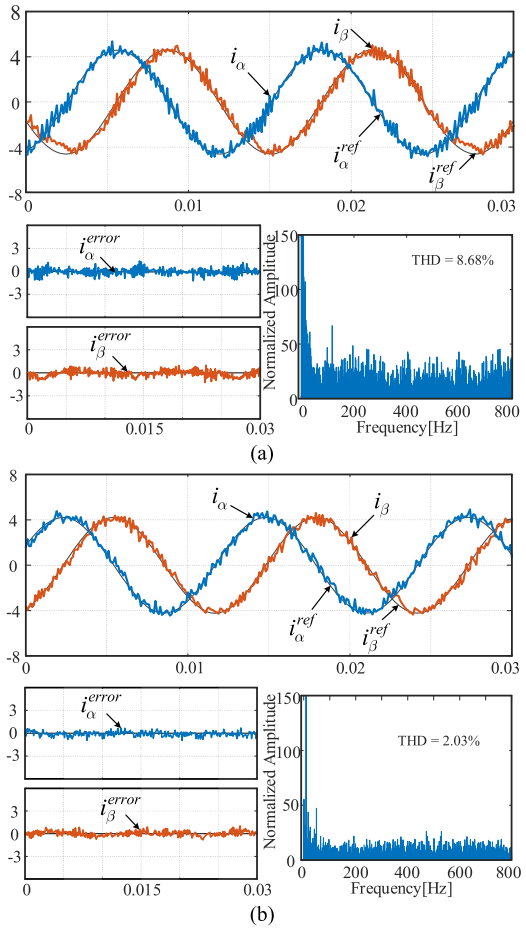

FIGURE 10. Current response under 1500 rpm and 3 Nm load-torque, (a) of the C-MFPCC and (b) of the proposed TVV-MFPCC. On the lower left of each part is the $\alpha\beta$ current errors and on the lower right of each part is the harmonic spectrum of α-phase current. Time is in seconds.

VI. EXPERIMENTAL VALIDATION

Experiments are conducted to assess the performance of the proposed TVV-MFPCC, and a comparative analysis against the C-MFPCC is carried out under steady-state and dynamic settings. To highlight the capability of the proposed controller, only current response is studied in the experiments. Three performance measures are defined for that purpose, including average current ripple (ACR), average current error (ACE), and total harmonic distortion (THD):

$$ACR = \sqrt{\frac{1}{N}\sum_{k=1}^{N}\left(i_x^{ref}(k) - i_x(k)\right)^2}, \quad x \in \{\alpha, \beta\} \tag{20}$$

$$ACE = \frac{1}{N}\sum_{k=1}^{N}\left|i_x^{ref}(k) - i_x(k)\right|, \quad x \in \{\alpha, \beta\} \tag{21}$$

$$THD = \frac{\sqrt{\sum_{n=2}^{50} i_{\alpha,n}^2}}{i_{1,\alpha,rms}} \tag{22}$$

where N represents the number of samples and n stands for the nth harmonic component.

A. EXPERIMENTAL SETUP

The experimental test bench is shown in Fig. 8, consisting of a three-phase SPMSM drive system and an inverter module. The system contains a power meter and a control unit, with specifications listed in Table 3. The inverter module circuit is made of various parts as indicated in the enlarged section: (A) A 32-bit floating TMS320F28379D dual-core microcontroller of Texas Instruments. (B) An overcurrent protection board and encoder circuit, (C) A power module inverter SCM1246MF with 6 low switching dissipation insulated gate bipolar transistors (IGBT), (D) LEM LA25-NP current sensors; (E) An A/D converter AD4001; (F) A current/voltage conversion circuit ADA4940; and (G) Capacitors rated 400V/10000μF.

The two controllers are evaluated experimentally using the same controller parameters, procedures, and operation conditions to yield fair and reasonable comparisons. There are two control loops in the experiment – current control and speed control. For the current control, no parameters are involved as the predictive controllers employed are model-free, but for the speed control, both the TVV-MFPCC and

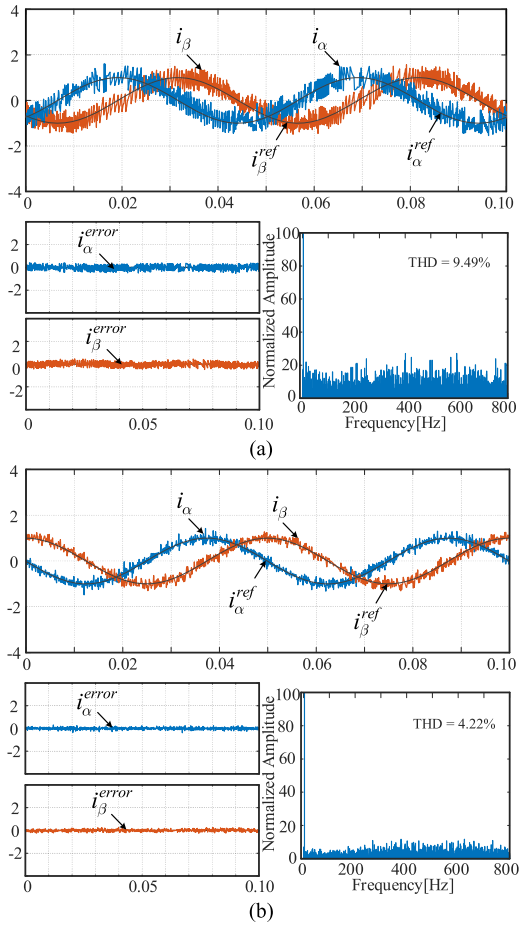

FIGURE 11. Current response under 1 A and 10 Hz, (a) of the C-MFPCC and (b) of the proposed TVV-MFPCC. On the lower left of each part is the $\alpha\beta$ current errors and on the lower right of each part is the harmonic spectrum of α-phase current. Time is in seconds.

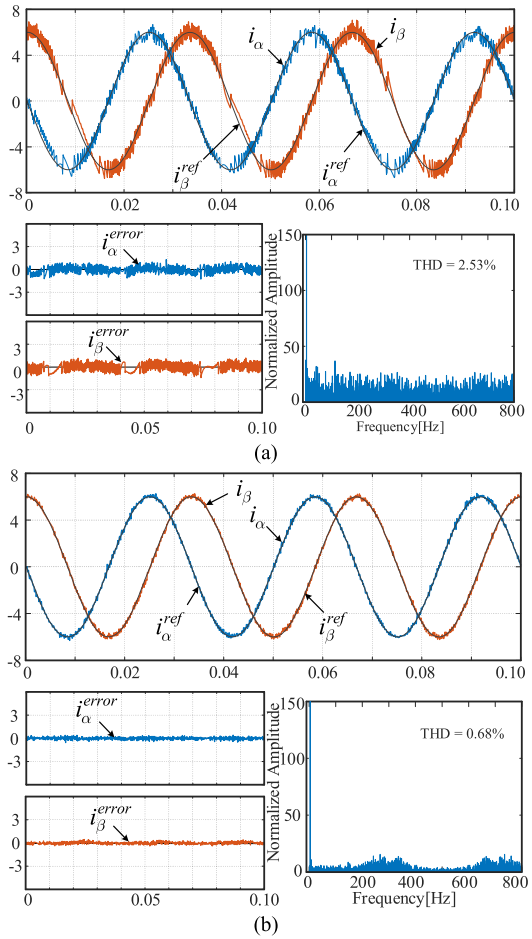

FIGURE 12. Current response under 6 A and 30 Hz, (a) of the C-MFPCC and (b) of the proposed TVV-MFPCC. On the lower left of each part is the $\alpha\beta$ current errors and on the lower right of each part is the harmonic spectrum of α-phase current. Time is in seconds.

the C-MFPCC use the same control gains k_p and k_i of a PI controller.

The sampling period is set as 100 μs. As shown in Table 4, the average calculation time of the proposed TVV-MFPCC and the conventional MFPCC are 56.8 μs and 32.4 μs, respectively. The increase is expected as the proposed controller applies three voltage vectors in a sampling period. Besides, rolling optimization of 16 candidate hybrid switching modes requires more computation as opposed to the C-MFPCC that only has 4 candidate switching states. However, the increase is still considered reasonable and viable under the sampling frequency.

B. STEADY-STATE PERFORMANCE

The steady-state performance is investigated. For speed control, the motor operates under the speed commands of 400 rpm (low speed) and 1500 rpm (high speed) with the same load torque of 3 Nm. The results are illustrated in Fig. 9-10. In addition to that, Fig. 11 shows the current response of 1 A at frequency 10 Hz, and Fig. 12 contains the current response of 6 A at frequency 30 Hz. The harmonic spectrum of α-phase is presented in each figure.

TABLE 5. Quantitative comparison of steady-state response.

Figure	C-MFPCC			TVV-MFPCC		
	ACR (A) [a]	ACE (A) [a]	THD (%) [b]	ACR (A) [a]	ACE (A) [a]	THD (%) [b]
9	0.62	0.51	11.37	0.33	0.27	6.86
10	1.27	1.01	8.68	0.42	0.35	2.03
11	0.31	0.26	9.49	0.13	0.10	4.22
12	0.48	0.39	2.53	0.14	0.11	0.68

[a]Average measured value of $\alpha\beta$.

[b]Measured value of α-phase only.

Compared to the C-MFPCC, the proposed TVV-MFPCC is observed to significantly reduce the average current ripples (ACR), average current errors (ACE), and total harmonic distortions (THD), as revealed from their waveform characteristics. Specifically, it can be observed from the enlarged section of Fig. 9 that the current waveforms of the proposed TVV-MFPCC are closer to the reference command than the C-MFPCC. The ACE is dropped from 0.51 A to 0.27 A, indicating that the prediction accuracy is improved by 47.06%. As depicted by Fig. 10, the measured ACR and ACE in

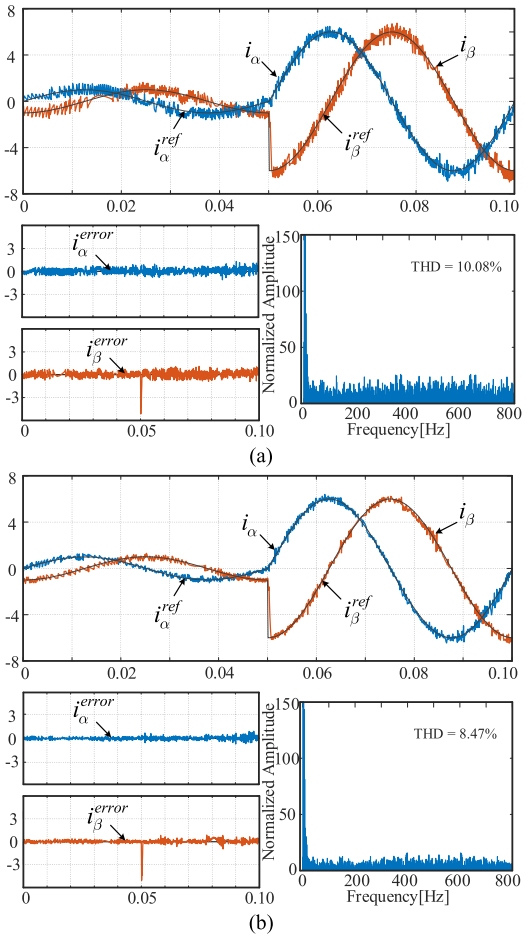

FIGURE 13. Dynamic current response under current jump from 1 A to 6 A at 10 Hz and load-torque of 2 Nm, (a) of the C-MFPCC and (b) of the proposed TVV-MFPCC. On the lower left of each part is the $\alpha\beta$ current errors and on the lower right of each part is the harmonic spectrum of α-phase current. Time is in seconds.

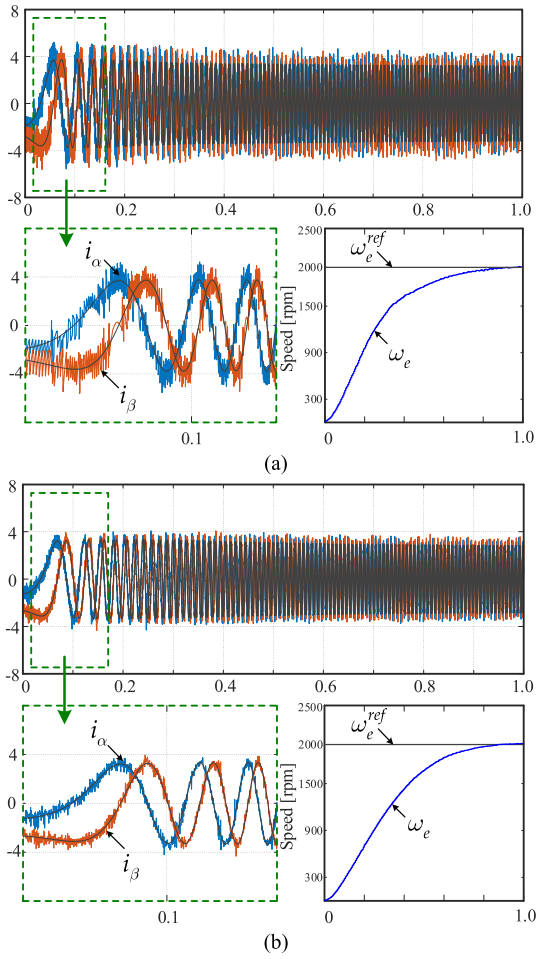

FIGURE 14. Dynamic current response from zero rpm to a 2000 rpm, (a) of C-MFPCC and (b) of the proposed TVV-MFPCC. On the lower left of each part is the enlarged $\alpha\beta$ current response, and on the lower right of each part is the speed response. Time is in seconds.

C-MFPCC is 0.62 A and 0.51 A, respectively, which are considerably higher than 0.33 A and 0.27 A, respectively, as of the proposed TVV-MFPCC. Similarly, in the harmonic spectrum, the THD of the proposed scheme is noticeably reduced by 39.67%. At a higher speed of 1500 rpm, the presented controller has shown a substantial improvement in its current ripples, as illustrated in Fig. 11. Compared to C-MFPCC, the proposed TVV-MFPCC has performed better with a significant decrease of the ACR, ACE, and THD by 66.93%, 65.35%, and 76.61%, respectively. Comparable results can be viewed in Fig. 12. Table 5 depicts the steady-state performance in terms of ACR, ACE, and THD. In general, the proposed TVV-MFPCC offers at least 50% improvement to errors and ripples. The THD, in particular, has been significantly reduced as high as 70%. The current tracking performance is experimentally evident.

C. DYNAMIC PERFORMANCE

In this experiment, three setups are considered: 1) current jump from 1 A to 6 A operating at frequency 10 Hz, 2) speed step from standstill to a rated speed of 2000 rpm, and 3) speed step from standstill to a low-speed command of 300 rpm. The test is aimed to assess the capability of the two controllers under dynamic conditions.

Fig. 13 shows the current response under current jump of 1 A to 6 A with an external load disturbance of 2 Nm. With the sudden change of stator current command at 50ms, the stator current jump to 6 A, causing the β-phase to drop quickly to 6 A. The proposed TVV-MFPCC is observed to yield smaller current ripples and current errors than does the C-MFPCC. To be more specific, a significant reduction in ACR and ACE by 32.50% and 45.16%, respectively, whereas the THD is dropped by 15.97% compared to the C-MFPCC.

The starting response from standstill to a speed command is illustrated in Fig. 14-15. This allows the machine to run from a full stop to a rated speed command of 2000 rpm and a lower speed command of 300 rpm. The machine is loaded with 2 Nm in both tests.

The starting response at a rated speed command is presented in Fig. 14. It is seen that both controllers experienced large current ripples and current errors, as evidently revealed by their current waveforms. However, current spikes are more

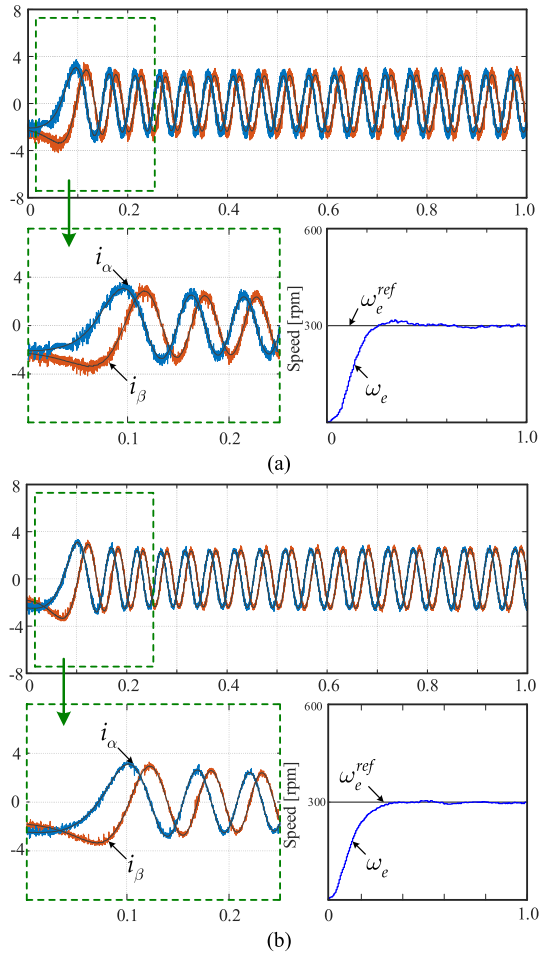

FIGURE 15. Dynamic current response under the condition from zero rpm to 300 rpm, (a) of the C-MFPCC and (b) of the proposed TVV-MFPCC. On the lower left of each part is the enlarged $\alpha\beta$ current response and on the lower right of each part is the speed response. Time is in seconds.

TABLE 6. Quantitative comparison of dynamic response.

Figure	C-MFPCC			TVV-MFPCC		
	ACR (A) [a]	ACE (A) [a]	THD (%) [b]	ACR (A) [a]	ACE (A) [a]	THD (%) [b]
13	0.40	0.31	10.08	0.27	0.17	8.47
14	0.88	0.71	14.09	0.56	0.45	6.68
15	0.39	0.21	4.55	0.16	0.13	1.32

[a]Average measured value of $\alpha\beta$.

[b]Measured value of α- phase only.

visible in the C-MFPCC, where current ripples obviously exceed 4 A. In contrast to that, the proposed TVV-MFPCC exhibits a more stable and smooth response. The ACR, ACE, and THD are improved by 36.36%, 36.62%, and 52.59%, respectively, compared to C-MFPCC in this test. The speed tracking of both controllers performs almost the same.

The dynamic response at lower speed command of 300 rpm is shown in Fig. 15. It is seen that the response at a sampling frequency of 10kHz is almost the same. However, the current ripples are distinguishably different – the TVV-MFPCC performs better against the C-MFPCC. The quantitative results under three dynamic conditions are summarized in Table 6.

VII. CONCLUSION

A triple-voltage-vector MFPCC is proposed to improve the performance of the four-switch three-phase (FSTP) inverter-fed SPMSM in this paper. Using the principle of discrete-space-vector modulation (DSVM), the proposed TVV-MFPCC has successfully mitigated voltage vector limitations. Three primary voltage vectors are linearly combined to generate sixteen candidate switching modes using four primary voltage vectors and twelve virtual voltage vectors. To effectively reduce current error, three switching modes are applied at equal application intervals in each sampling period, followed by three current readings and calculations of current differences. The average current differences are then used to generate current predictions. Experiments are conducted to assess the performance of the proposed TVV-MFPCC, and a comparison is made against C-MFPCC. The results show that the proposed method effectively improves current prediction accuracy under steady-state and dynamic test conditions, as evidently verified by a much smaller average current ripple (ACR), average current error (ACE), and total harmonic distortion (THD). Further study on the torque response is considered as our future work.

REFERENCES

[1] S.-K. Sul, *Control of Electric Machine Drive Systems*. Hoboken, NJ, USA: Wiley, 2011.

[2] W. Zhao, T. A. Lipo, and B.-I. Kwon, "Optimal design of a novel asymmetrical rotor structure to obtain torque and efficiency improvement in surface inset PM motors," *IEEE Trans. Magn.*, vol. 51, no. 3, pp. 1–4, Mar. 2015, doi: 10.1109/TMAG.2014.2362146.

[3] S.-K. Lee, G.-H. Kang, J. Hur, and B.-W. Kim, "Quasi-zero torque pulsation of surface permanent magnet synchronous motor for ship gyro stabilizer by pole/slot number and air-gap designs," *IEEE Trans. Magn.*, vol. 50, no. 2, pp. 797–800, Feb. 2014, doi: 10.1109/TMAG.2013.2284004.

[4] P. L. Chapman, S. D. Sudhoff, and C. A. Whitcomb, "Optimal current control strategies for surface-mounted permanent-magnet synchronous machine drives," *IEEE Trans. Energy Convers.*, vol. 14, no. 4, pp. 1043–1050, Dec. 1999, doi: 10.1109/60.815026.

[5] S. Morimoto, Y. Takeda, and T. Hirasa, "Current phase control methods for permanent magnet synchronous motors," *IEEE Trans. Power Electron.*, vol. 5, no. 2, pp. 133–139, Apr. 1990, doi: 10.1109/63.53150.

[6] C. Ruschetti, C. Verucchi, G. Bossio, C. De Angelo, and G. García, "Rotor demagnetization effects on permanent magnet synchronous machines," *Energy Convers. Manage.*, vol. 74, pp. 1–8, Oct. 2013, doi: 10.1016/j.enconman.2013.05.001.

[7] R. Errouissi, M. Ouhrouche, W.-H. Chen, and A. M. Trzynadlowski, "Robust cascaded nonlinear predictive control of a permanent magnet synchronous motor with antiwindup compensator," *IEEE Trans. Ind. Electron.*, vol. 59, no. 8, pp. 3078–3088, Aug. 2012, doi: 10.1109/TIE.2011.2167109.

[8] W. Zhang, D. Xu, P. N. Enjeti, H. Li, J. T. Hawke, and H. S. Krishnamoorthy, "Survey on fault-tolerant techniques for power electronic converters," *IEEE Trans. Power Electron.*, vol. 29, no. 12, pp. 6319–6331, Dec. 2014, doi: 10.1109/TPEL.2014.2304561.

[9] T. Tarczewski and L. M. Grzesiak, "Constrained state feedback speed control of PMSM based on model predictive approach," *IEEE Trans. Ind. Electron.*, vol. 63, no. 6, pp. 3867–3875, Jun. 2016, doi: 10.1109/TIE.2015.2497302.

[10] J. Rodriguez and P. Cortes, *Predictive Control of Power Converters and Electrical Drives*, 1st ed. West Sussex, U.K.: Wiley, 2012, pp. 133–143.

[11] M. Siami, M. Amiri, H. K. Savadkoohi, R. Rezavandi, and S. Valipour, "Simplified predictive torque control for a PMSM drive fed by a matrix converter with imposed input current," *IEEE J. Emerg. Sel. Topics Power Electron.*, vol. 6, no. 4, pp. 1641–1649, Dec. 2018, doi: 10.1109/JESTPE.2018.2837109.

[12] Q. N. Trinh, F. H. Choo, Y. Tang, and P. Wang, "Control strategy to compensate for current and voltage measurement errors in three-phase PWM rectifiers," *IEEE Trans. Ind. Appl.*, vol. 55, no. 3, pp. 2879–2889, May 2019, doi: 10.1109/TIA.2019.2894107.
[13] D. Zhou, X. Li, and Y. Tang, "Multiple-vector model-predictive power control of three-phase four-switch rectifiers with capacitor voltage balancing," *IEEE Trans. Power Electron.*, vol. 33, no. 7, pp. 5824–5835, Jul. 2018, doi: 10.1109/TPEL.2017.2750766.
[14] Z. Wu, J. Chu, W. Gu, Q. Huang, L. Chen, and X. Yuan, "Hybrid modulated model predictive control in a modular multilevel converter for multi-terminal direct current systems," *Energies*, vol. 11, no. 7, p. 1861, Jul. 2018, doi: 10.3390/en11071861.
[15] S.-J. Jeong and S.-H. Song, "Improvement of predictive current control performance using online parameter estimation in phase controlled rectifier," *IEEE Trans. Power Electron.*, vol. 22, no. 5, pp. 1820–1825, Sep. 2007, doi: 10.1109/TPEL.2007.904235.
[16] L. Xu, G. Chen, and Q. Li, "Ultra-local model-free predictive current control based on nonlinear disturbance compensation for permanent magnet synchronous motor," *IEEE Access*, vol. 8, pp. 127690–127699, 2020, doi: 10.1109/ACCESS.2020.3008158.
[17] M. Khalilzadeh, S. Vaez-Zadeh, and M. S. Eslahi, "Parameter-free predictive control of IPM motor drives with direct selection of optimum inverter voltage vectors," *IEEE J. Emerg. Sel. Topics Power Electron.*, vol. 9, no. 1, pp. 327–334, Feb. 2021, doi: 10.1109/JESTPE.2019.2949222.
[18] Z. Liu and Y. Zhao, "Robust perturbation observer-based finite control set model predictive current control for SPMSM considering parameter mismatch," *Energies*, vol. 12, no. 19, p. 3711, Sep. 2019, doi: 10.3390/en12193711.
[19] S.-C. Carpiuc and C. Lazar, "Fast real-time constrained predictive current control in permanent magnet synchronous machine-based automotive traction drives," *IEEE Trans. Transport. Electrific.*, vol. 1, no. 4, pp. 326–335, Dec. 2015, doi: 10.1109/TTE.2015.2482223.
[20] B. Wang, X. Chen, Y. Yu, G. Wang, and D. Xu, "Robust predictive current control with online disturbance estimation for induction machine drives," *IEEE Trans. Power Electron.*, vol. 32, no. 6, pp. 4663–4674, Jun. 2017, doi: 10.1109/TPEL.2016.2602853.
[21] M. Yang, X. Lang, J. Long, and D. Xu, "Flux immunity robust predictive current control with incremental model and extended state observer for PMSM drive," *IEEE Trans. Power Electron.*, vol. 32, no. 12, pp. 9267–9279, Dec. 2017, doi: 10.1109/TPEL.2017.2654540.
[22] J. Ren, Y. Ye, G. Xu, Q. Zhao, and M. Zhu, "Uncertainty-and-disturbance-estimator-based current control scheme for PMSM drives with a simple parameter tuning algorithm," *IEEE Trans. Power Electron.*, vol. 32, no. 7, pp. 5712–5722, Jul. 2017, doi: 10.1109/TPEL.2016.2607228.
[23] D. Su, C. Zhang, and Y. Dong, "Finite-state model predictive current control for surface-mounted permanent magnet synchronous motors based on current locus," *IEEE Access*, vol. 5, pp. 27366–27375, Nov. 2017, doi: 10.1109/ACCESS.2017.2771418.
[24] A. Abbaszadeh, D. A. Khaburi, H. Mahmoudi, and J. Rodríguez, "Simplified model predictive control with variable weighting factor for current ripple reduction," *IET Power Electron.*, vol. 10, no. 10, pp. 1165–1174, Aug. 2017, doi: 10.1049/iet-pel.2016.0483.
[25] C.-K. Lin, T.-H. Liu, J.-T. Yu, L.-C. Fu, and C.-F. Hsiao, "Model-free predictive current control for interior permanent-magnet synchronous motor drives based on current difference detection technique," *IEEE Trans. Ind. Electron.*, vol. 61, no. 2, pp. 667–681, Feb. 2014, doi: 10.1109/TIE.2013.2253065.
[26] C.-K. Lin, J.-T. Yu, Y.-S. Lai, and H.-C. Yu, "Improved model-free predictive current control for synchronous reluctance motor drives," *IEEE Trans. Ind. Electron.*, vol. 63, no. 6, pp. 3942–3953, Jun. 2016, doi: 10.1109/TIE.2016.2527629.
[27] M. Tomlinson, H. D. T. Mouton, R. Kennel, and P. Stolze, "A fixed switching frequency scheme for finite-control-set model predictive control—Concept and algorithm," *IEEE Trans. Ind. Electron.*, vol. 63, no. 12, pp. 7662–7670, Dec. 2016, doi: 10.1109/TIE.2016.2593997.
[28] S. Vazquez, J. I. Leon, L. G. Franquelo, J. Rodriguez, H. A. Young, A. Marquez, and P. Zanchetta, "Model predictive control: A review of its applications in power electronics," *IEEE Ind. Electron. Mag.*, vol. 8, no. 1, pp. 16–31, Mar. 2014, doi: 10.1109/MIE.2013.2290138.
[29] H.-C. Moon, J.-S. Lee, and K.-B. Lee, "A robust deadbeat finite set model predictive current control based on discrete space vector modulation for a grid-connected voltage source inverter," *IEEE Trans. Energy Convers.*, vol. 33, no. 4, pp. 1719–1728, Dec. 2018, doi: 10.1109/TEC.2018.2830776.
[30] I. Osman, D. Xiao, K. S. Alam, S. M. S. I. Shakib, M. P. Akter, and M. F. Rahman, "Discrete space vector modulation-based model predictive torque control with no suboptimization," *IEEE Trans. Ind. Electron.*, vol. 67, no. 10, pp. 8164–8174, Oct. 2020, doi: 10.1109/TIE.2019.2946559.
[31] K. S. Alam, M. P. Akter, D. Xiao, D. Zhang, and M. F. Rahman, "Asymptotically stable predictive control of grid-connected converter based on discrete space vector modulation," *IEEE Trans. Ind. Informat.*, vol. 15, no. 5, pp. 2775–2785, May 2019, doi: 10.1109/TII.2018.2876274.
[32] H. W. Van Der Broeck and J. D. Van Wyk, "A comparative investigation of a three-phase induction machine drive with a component minimized voltage-fed inverter under different control options," *IEEE Trans. Ind. Appl.*, vol. IA-20, no. 2, pp. 309–320, Mar. 1984, doi: 10.1109/TIA.1984.4504413.
[33] M. Amiri, J. Milimonfared, and D. A. Khaburi, "Predictive torque control implementation for induction motors based on discrete space vector modulation," *IEEE Trans. Ind. Electron.*, vol. 65, no. 9, pp. 6881–6889, Sep. 2018, doi: 10.1109/TIE.2018.2795589.

CRESTIAN ALMAZAN AGUSTIN was born in Isabela, Philippines, in 1989. He received the B.S. degree in electrical engineering from Isabela State University, Ilagan, Philippines, in 2012, the M.S. degree in engineering management from the University of La Salette, Santiago, Philippines, in 2015, and the M.S. degree in electrical engineering from the University of Saint Louis, Cagayan, Philippines, in 2017. He is currently pursuing the Ph.D. degree in electrical engineering with National Taiwan Ocean University, Keelung, Taiwan. His research interests include control of motor drives and inverter topologies.

JEN-TE YU was born in Hualien, Taiwan. He received the M.S. degree in aerospace engineering from Wichita State University, USA, the M.S. degree in electrical engineering from the Georgia Institute of Technology, USA, and the Ph.D. degree in electrical engineering from National Taiwan University, Taiwan.

He has been with the Department of Electrical Engineering, Chung Yuan Christian University (CYCU), Taiwan, as an Assistant Professor, since August 2016, where he currently serves as the Director of the Modern Control Laboratory. Before joining CYCU, he had worked in the industry for years both in the U.S. and Taiwan, as an Engineer and later as a Corporate Research and Development Manager. His current research interests include networked control subject to sporadic packet dropout, linear quadratic regulator theory, consensus of multiagent systems, and output feedback design of negative imaginary systems.

CHENG-KAI LIN was born in Taipei, Taiwan, in 1980. He received the B.S. degree in electrical engineering from the Ming Chi University of Technology, Taipei, Taiwan, in 2002, and the M.S. and Ph.D. degrees in electrical engineering from the National Taiwan University of Science and Technology, Taipei, in 2004 and 2009, respectively.

From October 2009 to August 2012, he was a Postdoctoral Researcher with the Department of Electrical Engineering, National Taiwan University, Taipei. He is currently an Associate Professor of electrical engineering with National Taiwan Ocean University, Keelung, Taiwan. His research interests include motor drive control, power electronic applications, and control applications.

JUNG JAI was born in Hsinchu, Taiwan, in 1995. He received the B.S. degree in automatic control engineering from Feng Chia University, Taichung, Taiwan, in 2018, and the M.S. degree in electrical engineering from National Taiwan Ocean University, Keelung City, Taiwan, in 2020. His research interest includes motor control and applications.

YEN-SHIN LAI (Fellow, IEEE) received the M.S. degree in electronic engineering from the National Taiwan University of Science and Technology, Taipei, Taiwan, and the Ph.D. degree in electronic engineering from the University of Bristol, Bristol, U.K.

In 1987, he joined the Department of Electrical Engineering, National Taipei University of Technology, Taipei, where he served as the Chairperson, from 2003 to 2006, and has been a Full Professor, since 1999, a Distinguished Professor, since 2006, and a Chair Professor, since 2013. His research interests include the control of power converters, inverters, and motor drives.

Dr. Lai received several national and international awards, including the John Hopkinson Premium for the session 1995–1996 from the Institute of Electrical Engineers (IEE), Technical Committee Prize Paper Award from the IEEE IAS Industrial Drives Committee for 2002, the Outstanding Paper Award from the International Conference of Renewable Energy Research and Applications, Nagasaki, Japan, in 2012, and the Best Paper Award from the IEEE PEDS, Kitakyushu, Japan, 2013. He received the Outstanding Research Award from the Ministry of Science and Technology, Taiwan, in 2013 and 2018. He was also awarded the 2018 Prize Paper Award from the IEEE JOURNAL OF EMERGING AND SELECTED TOPICS IN POWER ELECTRONICS, TECO Award, in 2019, and the Award for Industry Collaboration from the Ministry of Education, Taiwan, in 2020. He served as the Secretary of IEEE IAS Industrial Drives Committee, from 2008 to 2009, and the Chapter Chair of IEEE IAS Taipei Chapter, from 2009 to 2010. He served as the Vice-Chair (2010–2013) and the Chair (2014-2015) for IEEE IAS Industrial Drives Committee. He also served as an Associate Editor for IEEE TRANSACTIONS ON INDUSTRY APPLICATIONS, from 2008 to 2011, IEEE TRANSACTIONS ON INDUSTRIAL ELECTRONICS, and *IET Electrical Power Applications*. He also served as the Chair for the Electrical Power Engineering Division, Ministry of Science and Technology, Taiwan, and the President of Taiwan Power Electronics Association, Taiwan, from 2016 to 2019. He is currently an elected AdCom Member of IEEE Industrial Electronics Society, since 2011, an Editor of IEEE JOURNAL OF EMERGING AND SELECTED TOPICS IN POWER ELECTRONICS, and the Co-Editor-in-Chief of IEEE TRANSACTIONS ON INDUSTRIAL ELECTRONICS.